Title: Controllable synthesis, XPS investigation and magnetic property of multiferroic BiMn2O5 system: The role of neodyme doping

Author: H. Felhi, M. Smari, Anna Bajorek, K. Nouri, E. Dhahri, L. Bessais

Citation style: Felhi H., Smari M., Bajorek Anna, Nouri K., Dhahri E., Bessais L. (2019). Controllable synthesis, XPS investigation and magnetic property of multiferroic BiMn2O5 system: The role of neodyme doping. "Progress in Natural Science: Materials International" (Vol. 29 (2019), s. 198–209), doi 10.1016/j.pnsc.2019.04.001

Controllable synthesis, XPS investigation and magnetic property of multiferroic BiMn$_2$O$_5$ system: The role of neodyme doping

H. Felhi[a,*], M. Smari[a,b], A. Bajorek[c,d], K. Nouri[e], E. Dhahri[a], L. Bessais[e]

[a] Applied Physics Laboratory, Sfax Faculty of Sciences, University of Sfax, B.P. 1171, Sfax 3000, Tunisia
[b] Center for Functionalized Magnetic Materials (FunMagMa), Immanuel Kant Baltic Federal University, 236041, Kaliningrad, Russia
[c] A. Chełkowski Institute of Physics, University of Silesia in Katowice, 75 Pułku Piechoty 1, 41-500 Chorzów, Poland
[d] Silesian Center for Education and Interdisciplinary Research, University of Silesia in Katowice, 75 Pułku Piechoty 1A, 41-500 Chorzów, Poland
[e] CMTR, ICMPE, UMR 7182 CNRS-UPEC, 2 rue Henri Dunant, F-94320 Thiais, France

ARTICLE INFO

ABSTRACT

In this work, a novel series of multiferroic materials BiMn$_2$O$_5$ doped by Neodyme has been prepared by a sol-gel method at low temperature. The crystallographic studies using X-ray diffraction and Rietveld Refinement techniques showed the formation of single-phase samples for all compositions, crystallizing in a mullite-type orthorhombic perovskite structure, space group Pbam (Z = 4). The SEM techniques confirmed the formation of single-phase materials with excellent mapping distribution. Raman and infrared spectroscopic measurements were performed and combined with lattice dynamics simulations to describe the room-temperature vibrational properties of all samples. The X-ray Photoelectron Spectroscopy (XPS) were measured in the energy range of 0–1400 eV at room temperature. The Fermi level E$_F$ was defined with the accuracy of 0.127, 0.32 and 0.48 eV for BiMn$_2$O$_5$, Bi$_{0.9}$Nd$_{0.1}$Mn$_2$O$_5$ and Bi$_{0.8}$Nd$_{0.2}$Mn$_2$O$_5$ respectively. The X-ray photoelectron spectroscopy shows the existence of Mn^{4+} state. Magnetic measurements indicate Neél temperature T$_N$ at 31, 40 and 61 K for BiMn$_2$O$_5$, Bi$_{0.9}$Nd$_{0.1}$Mn$_2$O$_5$ and Bi$_{0.8}$Nd$_{0.2}$Mn$_2$O$_5$ respectively.

1. Introduction

Smart materials are sensitive to external stimuli such as stress, temperature, and electric or magnetic field. Thus, several technological inputs are expected. Multiferroic materials belong to these kinds of smart materials when their ferroelectric properties can be tuned by applying a magnetic field, indicating the existence of an effective magnetoelectric coupling [1]. Recently, two novel classes of multiferroic materials in which ferroelectricity can be triggered by either magnetic ordering [2] or charge ordering [3] have emerged. Tremendous work has been devoted to these novel classes of materials, and structural RMn$_2$O$_5$ (R = rare earth, La, Y or Bi) insulators [4,5] are typical examples. The crystals of the series RMn$_2$O$_5$ (R^{3+}Mn^{3+}Mn^{4+}O$_5$$^{2-}$, where R^{3+} denotes a rare-earth ion or Bi^{3+}) belong to the class of magnetoelectric crystals, for which magnetic and structural phase transitions take place at the same temperature T ~ 40 K [6–9]. At room temperature, these crystals have orthorhombic symmetry described by the space group Pbam, have attracted considerable attention due to their multiferroic properties such as magnetoelectricity and magnetodielectricity [10].

In the mean structure, there are two distinct crystallographic sites

for Mn^{4+} (site 4f) and Mn^{3+} (site 4 h) forming Mn^{3+}O$_5$ square pyramids, and corner sharing Mn^{4+}O$_6$ octahedra are coordinated to eight oxygen atoms forming BiO$_8$ polyhedra. These polyhedra are responsible for the inter connection between both manganese cations localized at the octahedral and tetragonal pyramidal sites [11]. The mixed valence manganese ions occupying different crystallographic sites lead to the formation of a magnetic structure with two different magnetic sublattices. As one representative group of these special multiferroic materials, they have been immensely investigated in recent years [12,13].

This paper aims, firstly, to demonstrate that the sol gel is an adequate synthesis method to obtain multiferroic materials and, secondly, to investigate the role of the Neodyme ions as improving dopants and their effect on the physical properties in multiferroics material. Therefore, this study demonstrates the potential of X-ray photoelectron spectroscopy as a tool to study valence and magnetic state of ions in compounds.

2. Experimental section

The Nd^{3+} substituted bismuth compounds with the general formula

---

* Corresponding author.
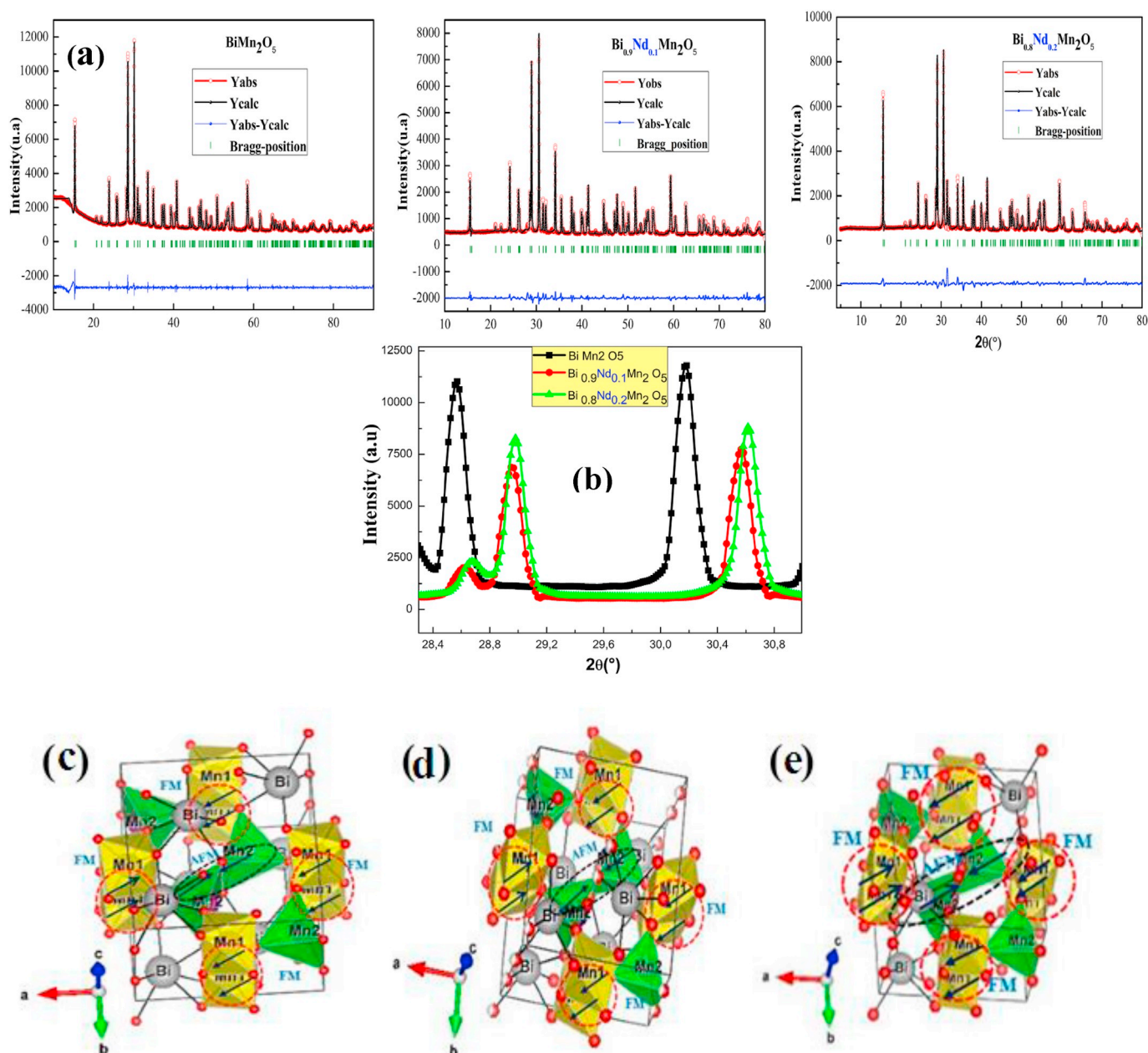 E-mail address: houdafelhi@yahoo.com (H. Felhi).

Fig. 1. (a) X-ray diffraction pattern for three samples. (b) XRD pattern of two main peaks. (c), (d) and (e) approximation of $BiMn_2O_5$, $Bi_{0.9}Nd_{0.1}Mn_2O_5$ and $Bi_{0.8}Nd_{0.2}Mn_2O_5$ unit cell respectively, presenting $Mn^{4+}O_6$ octahedra and Mn^{3+} pyramids.

$Bi_{1−x}Nd_xMn_2O_5$ (x = 0, 0.1 and 0.2) were obtained as a black poly-crystalline powder starting from precursors previously synthesized by a sol gel technique. The stoichiometric amounts of analytical grade (Bi $(NO_3)_3·5H_2O)$, $(Mn(NO_3)_2·4H_2O)$ and Nd_2O_3 were solved in Citric acid. The citrate solutions were slowly evaporated and decomposed at temperatures up to 600 °C. All the organic materials were eliminated in a subsequent treatment at 800 °C in air. The sample was finally annealed at 850 °C in air for 24 h [14]. Powder XRD patterns at room temperature were collected with a Cu $K\alpha_1(1.5406 Å)$. All diffraction patterns have been refined with the Rietveld refinement method [15] using FULLP-ROF program. The background was fitted with a 12-coefficient poly-nomial function, and the peak shapes were simulated by a pseudo-Voigt function. In the final run, the following parameters were refined: zero points, U, V, W, background points, scale factor, unit cell parameters, positional parameters, isotropic thermal factors and preferred orienta-tion parameters. Unique isotropic atomic displacement parameters were used for all oxygen positions in all refinements.

Scanning electron microscopy (SEM) was performed with a Rigaku JSM- 6700F microscope operated at 10 kV.

The composition and chemical states of surface elements of samples were investigated by X-ray photoelectron spectroscopy (XPS) (PHI 5700/660 Physical Electronics), using Al K-alpha (1486.6 eV) as the X-ray source. The surfaces are etched by an Ar^+ ion beam for 30 min to remove surface contamination. The survey spectra were collected with the pass energy 187.85eV. The studied spectra were analyzed using MultiPak 9.2 program according to the C1s peak, which was used as a reference for charge correction. All collected core level lines spectra during XPS examinations were measured with a standard limit of re-solution 0.1eV.

The Raman scattering spectra were excited with the 514.5 nm laser line from an Ar^+ laser, with a power of $\sim$ 12 mW focused in a spot of $\sim$ 100μ m diameter. Room temperature infrared reflectivity has been measured using Fourier transform infrared spectrometer (Vertex 80v) at near-normal incidence mode.

Table 1
Structural parameters.

Samples	$BiMn_2O_5$	$Bi_{0.9}Nd_{0.1}Mn_2O_5$	$Bi_{0.8}Nd_{0.2}Mn_2O_5$
Space group	Pbam	Pbam	Pbam
a(Å)	7.54946	7.450565	7.439506
b(Å)	8.54962	8.419172	8.423370
c(Å)	5.753627	5.682965	5.673781
v(Å³)	371.3679	356.4786	355.5516
Z	4	4	4
χ^2	2.42	4.62	3.81
$Mn^{4+}O_6$			
Mn1−O2	1.902	1.893	1.833
Mn1−O4	1.945	1.896	1.841
Mn1−O3	1.856	1.86	1.746
< Mn−O >	1.901	1.883	1.806
$Mn^{3+}O_5$			
Mn2−O1	1.905	1.833	1.852
Mn2−O2	1.941	1.917	1.948
Mn2−O3	2.10	2.01	2.17
< Mn−O >	1.982	1.92	1.99
$<r_A>$ Å	1.03	1.043	1.056
$<\sigma_A^2>$ Å²	0	0.001521	0.002704
Scherrer method (D) (nm)	47.74	47.079	44.79
$\delta \times 10^{-4}(nm^{-2})$	2.66	3.105	3.369
ε%	0.282	0.2757	0.2931
Average grain size (S_{MEB}) (nm)	107	103	92
X-ray density (g cm⁻³)	7.1331137	7.3112	7.209
Bulk density (g cm⁻³)	5.03331137	4.85429	4.62685
Porosity	0.2943	0.33604	0.35818

The dc magnetization measurements were made in a 500 Oe SQUID magnetometer (Quantum Design, MPMS). First, zero-field-cooled (ZFC), Field-cooled warning (FCW) and field-cooled (FC) magnetization curves were measured to determine the Néel temperature (T_N), which is sensitive to the grain-size distribution. The ZFC curves were obtained by cooling the sample under a zero field from 300 K to 2 K, and subsequently sweeping the temperature from 2 K to 300 K under a weak applied field. Then, hysteresis loops for the studied multiferroics samples were measured at different temperatures, and applied magnetic field up to 7T.

3. Results and discussions

3.1. X-ray diffraction (XRD) study

The X-ray diffraction data (XRD) of the three samples were refined by the Rietveld method. Fig. 1 (a) shows a good agreement between the calculated and observed data for the patterns of parent ($BiMn_2O_5$) as well as the neodyme-substituted samples $Bi_{1-x}Nd_xMn_2O_5$ with (x = 0,

0.1 and 0.2) collected at room temperature. The entire XRD pattern reveals a well-crystallized orthorhombic phase with space group *Pbam* [14]. In these structures, Mn ions are found in two different crystallographic sites: Mn^{4+} ions occupy the octahedral pyramidal site (4f) coordinated with six oxygen atoms and Mn^{3+} ions at a tetragonal pyramidal site (4 h) with five oxygen atoms. The Bi^{3+} ions sites at the 4 g sites are coordinated to eight oxygen atoms forming BiO_8 polyhedra [16–18]. The Rietveld refinement was done using FULLPROF software [19] to study the detailed crystal structure and the fitting parameters are listed in Table 1. The substitution of Nd^{3+} ions having lower ionic radius than that of Bi^{3+} ions results in the reduction of lattice parameters and cell volume [20] as seen from Table 1. A closer view of the obtained XRD peaks around 28–31° in Fig. 1(b) shows a slight shifting of the main peaks i.e. (121) and (211) to higher 2θ angles with the increase in x concentration. This feature can also be attributed to lower ionic radii substitution, thus confirming the substitution of Nd^{3+} ions at Bi^{3+} site [21]. Besides, the variation in bipyramid and octahedral coordinated Mn−O bond lengths due to substitution are estimated and listed in Table 1. Fig. 1 (c), (d) and (e) represent a schematic representation of the crystallographic structure. In this representation distorted $Mn^{4+}O_6$ octahedron is the environment of the Mn^{4+} (Mn_1 atoms), which forms infinite linear chains along the c-axis, sharing edges via the O_3 and O_4 oxygen. Mn^{3+} (Mn_2 atoms) occupy $Mn^{3+}O_5$ distorted tetragonal pyramids and have five oxygen atoms as neighbors. Moreover, the comparative variation of Mn_1−O as well as Mn_2−O bond lengths in $Bi_{1-x}Nd_xMn_2O_5$ with (x = 0, 0.1 and 0.2) are schematically depicted in Fig. 2 (a), (b) and (c), respectively. All the refinement results, the average ion radius of the A cation site $< r_A >$ and the mismatch σ^2 for all our samples are also listed in Table 1.

The average crystallite size estimated from XRD data using Scherrer's formula and the cell volume of all samples are estimated and shown in Table 1.

The Scherrer's formula can be written as [22]:

$$D= \frac{\lambda.k}{\beta\cos\theta} \tag{1}$$

where constant k depends upon the shape of the crystallite size (k = 0.9), (assuming the circular grain), β, Full Width at Half Maximum (FWHM) of intensity vs 2θ profile, λ is the wavelength of the Cu $K\alpha_1$ radiation (0.15406 nm) and θ is the Bragg diffraction angle of the most intense peak.

It is found that the average crystallite size of $Bi_{1-x}Nd_xMn_2O_5$ with (x = 0.1 and 0.2) are less than that of the fraction (x = 0). Earlier, it was reported that the unit cell parameter decreases as the average crystallite size decreases [23]. The dislocation density δ, which represents the amount of defects in the sample is defined as the length of
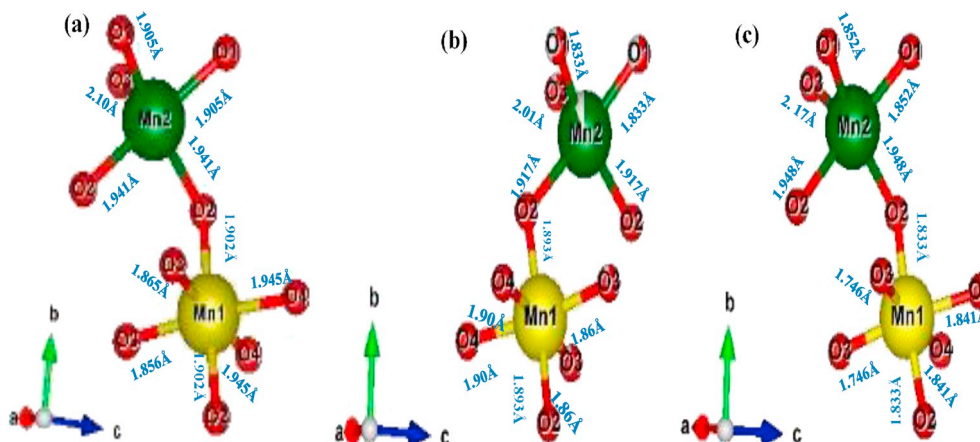

Fig. 2. The Mn−O backbone of the pyramid and octahedron in the structures of (a) $BiMn_2O_5$, (b) $Bi_{0.9}Nd_{0.1}Mn_2O_5$ and (c) $Bi_{0.2}Nd_{0.1}Mn_2O_5$ samples.
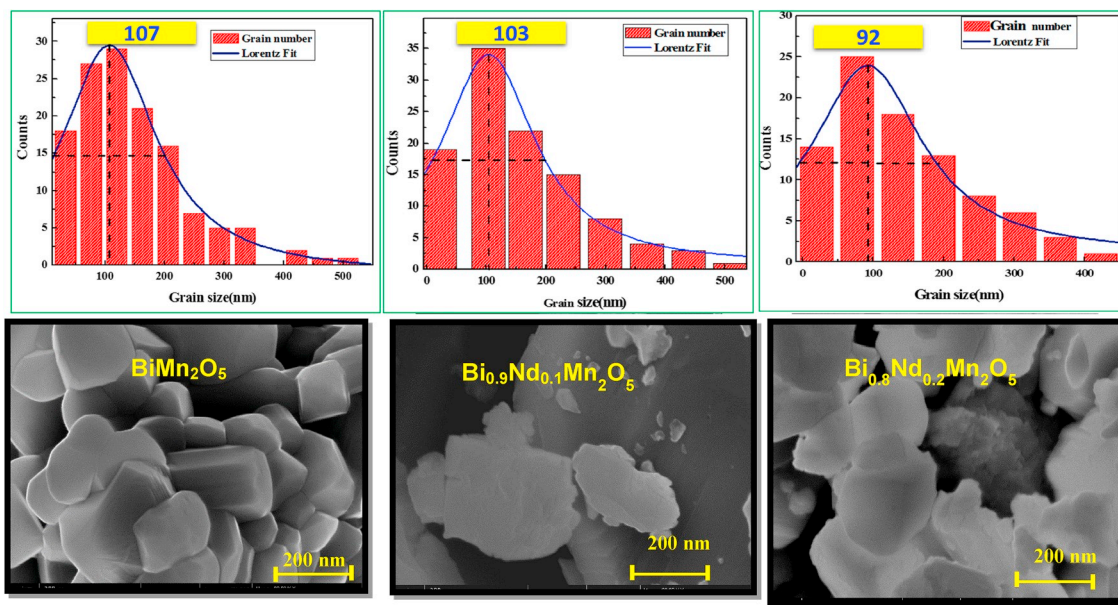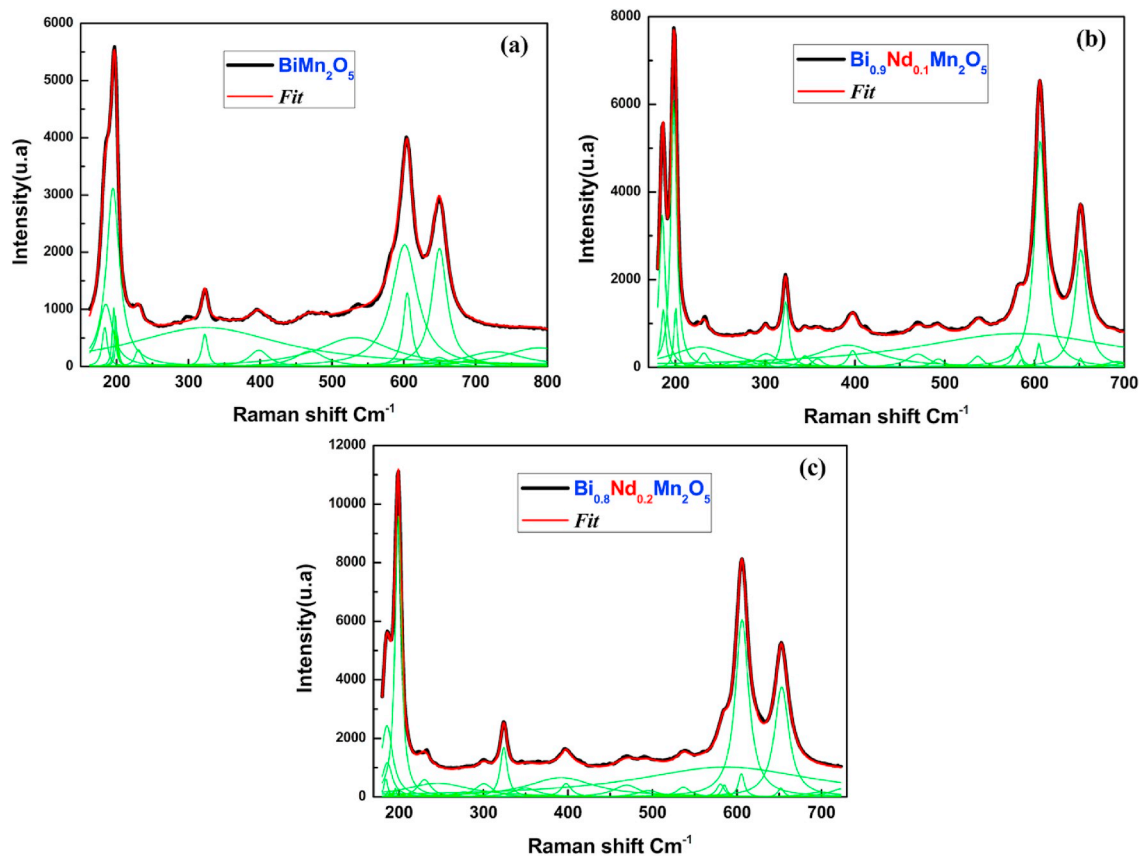
Fig. 3. SEM micrographs of all samples.

Fig. 4. Unpolarized Raman spectra of the multiferroic systems at room temperature.

Table 2
Structural parameters obtained from the raman of the room-temperature for $BiMn_2O_5$.

Sample	Center (Cm^{-1})	Height (u.a)	Area (cm^2)	FWHM(cm)
$BiMn_2O_5$	183	690.269	9253.09	8.53392
	185	1088.92	40723	23.8081
	195	3121.19	107442	21.9147
	196	1041.94	8082.46	4.93833
	198	901.631	5998.63	4.23549
	200	580.943	4653.45	5.09944
	230	298.697	5606.43	11.9491
	323	568.41	8665.92	9.70583
	324	681.198	281746	263.308
	398	286.838	14626.9	32.4634
	469	269.91	21582.1	50.9044
	532	507.529	100306	125.819
	601	2132.23	143756	42.9214
	604	1289.48	27456.8	13.5554
	649	159.523	8791.69	35.0857
	650	2064.52	83077.9	25.618
	693	111.37	7439.96	42.5288
	726	258.885	42040.9	103.382
	788	327.673	61384	119.26

Table 3
Structural parameters obtained from the raman of the room-temperature for $Bi_{0.9}Nd_{0.1}Mn_2O_5$.

Sample	Center(Cm-1)	Height (u.a)	Area(cm2)	FWHM(cm)
$Bi_{0.9}Nd_{0.1}Mn_2O_5$	185	3489.06	44197.8	8.0644
	186	1325.77	12855.7	6.1732
	198	6095.33	73337.1	7.65961
	200	1384.51	9566.92	4.39902
	228	461.51	60691.1	83.7189
	231.	328.055	6608.93	12.8252
	266	130.321	5711.58	27.9011
	282	156.457	4317.9	17.5694
	300	168.47	1844.69	6.97079
	301	306.94	14970.3	31.0497
	322	1497.51	21030.8	8.94058
	344	261.485	6055.4	14.7426
	358	197.097	4480.82	14.4729
	391	130.319	6535.55	31.9268
	397	385.751	7027.52	11.5978
	470	300.07	14281	30.2982
	492	192.524	4986.99	16.4905
	536	253.916	6073.41	15.2273
	580	489.349	7558.61	9.83339
	582	770.992	346259	285.911
	585	178.135	1593.72	5.69563
	604	560.419	4744.14	5.3892
	606	5167.75	123580	15.2239
	651	212.263	1867.47	5.60094
	652	2687.04	68719.5	16.2812
	691	130.319	6535.55	31.9268
	719	253.41	13161.5	33.0644

dislocation lines per unit volume of the crystal and is calculated using the Eq:

$$\delta = \frac{1}{D^2} \qquad (2)$$

The strain-induced broadening in powders due to crystal imperfection and distortion was calculated using the formula,

$$\varepsilon = \frac{\beta_{hkl}}{4\tan\theta} \qquad (3)$$

The values of the dislocation density δ and the strain ε are listed in

Table 1. Various structural parameters, like X-ray density, measured density and porosity were determined with the help of XRD data using the following mathematical relations [24]:

$$\rho_m = \frac{m}{\pi r^2 h} \qquad (4)$$

With m the mass of the pellet, r is the radius and h is the thickness of the pellet.

$$\rho_{X-ray} = \frac{ZM}{N_A V_{cell}} \qquad (5)$$

In Eq. (5), M is the molar mass, the value of Z (number of formula units per unit cell) is 4 for orthorhombic system and V_{cell} is the cell volume (Table 1).

$$P = 1 - \frac{\rho_m}{\rho_{X-ray}} \qquad (6)$$

In Eq. (6), P is the porosity, ρ_{X-ray} is the X-ray density and ρ_m is the bulk density.

It is further observed that ρ_{X-ray} and P increase with the increase in the concentration of Nd^{3+} ion [25].

3.2. Surface analysis by SEM

At the same time, the surface morphology and size of the grains of our compounds were examined using Scanning Electron Microscopy (SEM) images using the Image-J software.

The SEM images of the Grain size distribution of $Bi_{1-x}Nd_xMn_2O_5$ (x = 0, x = 0.1 and x = 0.2), respectively, are shown in Fig. 3. The average particle size, commonly known as grain, was 107 nm for $BiMn_2O_5$, 103 nm for $Bi_{0.9}Nd_{0.1}Mn_2O_5$ and 92 nm for $Bi_{0.8}Nd_{0.2}Mn_2O_5$ [14]. In addition, the grain growth and crystallization is observed with decreasing neodymium substitution. Obviously, the grain sizes observed by SEM are several times larger than those calculated by XRD, which indicates that each grain observed by SEM is composed of several crystallites [26].

3.3. Raman spectroscopy study

To have better insight to the vibrational, structural and lattice properties, the room-temperature Raman spectra of the parent ($BiMn_2O_5$) and its substituted samples ($Bi_{0.9}Nd_{0.1}Mn_2O_5$ and $Bi_{0.8}Nd_{0.2}Mn_2O_5$) were performed at wave number ranging from 100 to 800 cm^{-1} are illustrated in Fig. 4(a), (b) and (c). Factor group analysis for the *Pbam* symmetry of the paraelectric phase of these oxides yields 48 Raman-active phonon modes ($\Gamma_{Raman} = 13A_g + 13B_{1g} + 11B_{2g} + 11B_{3g}$) [27]. The A_g modes are expected to appear in the parallel xx, yy and zz scattering configuration and should not be seen in the crossed *xy, xz* and *yz* configurations. The B_{1g}, B_{2g} and B_{3g} modes are expected in xy, xz and yz configurations, respectively. The room-temperature and temperature-dependent Raman spectra for the RMn_2O_5 family of materials have been reported by various groups [28]. Raman modes have been observed, except few whose intensities are either very small or exist at < 100 cm^{-1}. Briefly, Raman studies indicate that the Nd substitution does not significantly change the phonon structure of the parent compound except for a change in the wave number and broadening of the phonon pattern due to Nd substitution. To clearly assign the active Raman modes, we have deconvoluted the Raman spectra of three samples. The deconvolution of Raman peaks of all samples was realized with the Fityk software by Lorentzian A function in the form $I = Io + \sum A_i \tau_i / [4(\omega - \omega_i)^2 + \tau_i^2]$ where, i is the peak number, Io is the background intensity, ω_i is the center frequency, τ_i is the full width at half maxima (FWHM), and A_i is the area of ith of the peak [29]. The

Table 4
Structural parameters obtained from the raman of the room-temperature for $Bi_{0.2}Nd_{0.2}Mn_2O_5$.

Sample	Center(Cm^{-1})	Height (u.a)	Area(cm^2)	FWHM(cm)
$\textbf{Bi}_{0.8}\textbf{Nd}_{0.2}\textbf{Mn}_2\textbf{O}_5$	184	642.185	5407.7	5.36083
	185	2444.5	62583	16.2985
	186	1174.93	26399	14.304
	187	192.622	1250.11	4.13165
	195	302.363	1261.53	2.65612
	196	233.662	3777.91	10.293
	199	9613.59	131431	8.70345
	230	590.082	17849.2	19.2569
	245	469.959	70275.5	95.1973
	277	172.026	7907.14	29.2621
	300	452.781	18192.2	25.5786
	324	1703.37	26910	10.0574
	349	305.769	17208	35.8275
	392	658.258	101096	97.7723
	397	461.162	10871.3	15.0074
	469	404.01	24078.7	37.942
	494	222.583	10876	31.107
	536	333.178	10437	19.9425
	580	442.995	7660.56	11.0089
	585	418.867	4944.39	7.51479
	586	1019.83	421279	262.979
	604	802.143	10471.6	8.31079
	606	6052.1	183535	19.306
	651	311.004	3998.03	8.18388
	652	3875.58	112859	18.5387
	653	3765.44	122735	20.7506
	699	2.90249	622.881	136.62
	723	274.965	15032.5	34.8043

deconvoluted Raman spectra of $BiMn_2O_5$ with 19 major Raman modes [30], for $Bi_{0.9}Nd_{0.1}Mn_2O_5$, there are 27 Raman peaks and for $Bi_{0.8}Nd_{0.2}Mn_2O_5$, there are 28 Raman peaks. The missing modes are of very low intensity or superimposed or out of the spectral range (< 100 cm^{-1}) of our Raman setup. Their positions are summarized in Tables 2–4.

Fig. 5 (a), (b) and (c) show the IR spectra at room temperature for all samples. It is a complementary technique to Raman spectroscopy. They are both from the same physical origin, either the interaction of light with the phonons or the vibration of the atomic bonds of a molecule that satisfies the permissible transitions between the different levels of vibrational energy. The different nature of the two processes of Raman and infrared interaction means that some vibrations will only be active in Raman, others are only active in infrared and others will be active for both. It can be seen that the relative peaks are added to the infrared and Raman curve corresponding to the Nd group vibration modes.

3.4. X-ray photoelectron spectroscopy (XPS) study

A typical, low-resolution X-ray photoelectron survey spectrum for $BiMn_2O_5$, $Bi_{0.9}Nd_{0.1}Mn_2O_5$ and $Bi_{0.8}Nd_{0.2}Mn_2O_5$ before etching and after etching by Ar beam respectively, in the energy range of 0–1400 eV are shown in Fig. 6. XPS did not reveal any traces of impurities besides, carbon accumulated on the surface. The strongest peaks of Bi $4f_{7/2}$, Bi $4f_{5/2}$, Bi $5d_{3/2}$, Bi $5d_{5/2}$, Mn $2p_{3/2}$, Mn $2p_{1/2}$, O 1s, C 1s and Nd $3d_{5/2}$ were chosen for investigating peculiarities of the core-level XPS spectra in these quasi-one-dimensional semiconductors. Fig. 7 (a) shows the valence band (VB) spectra for all samples, whose main features are indicated by ticks.
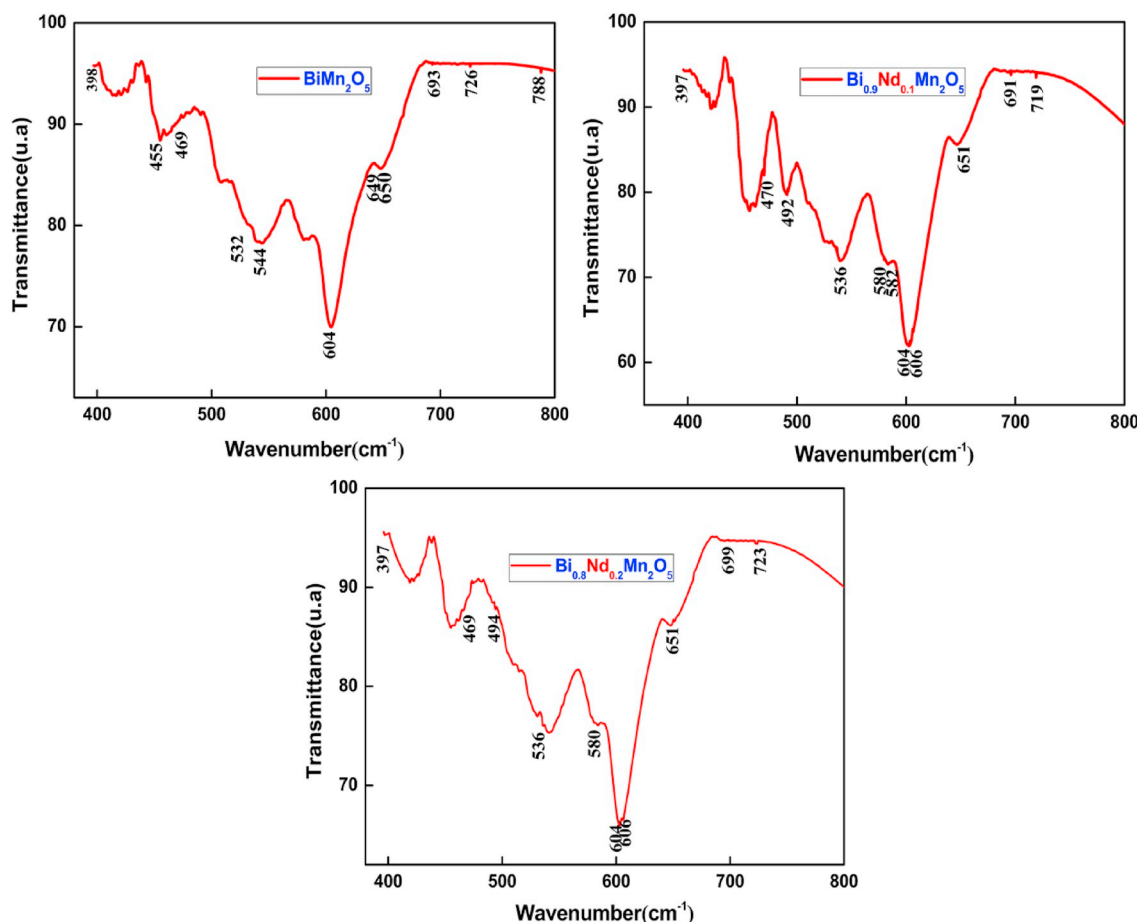

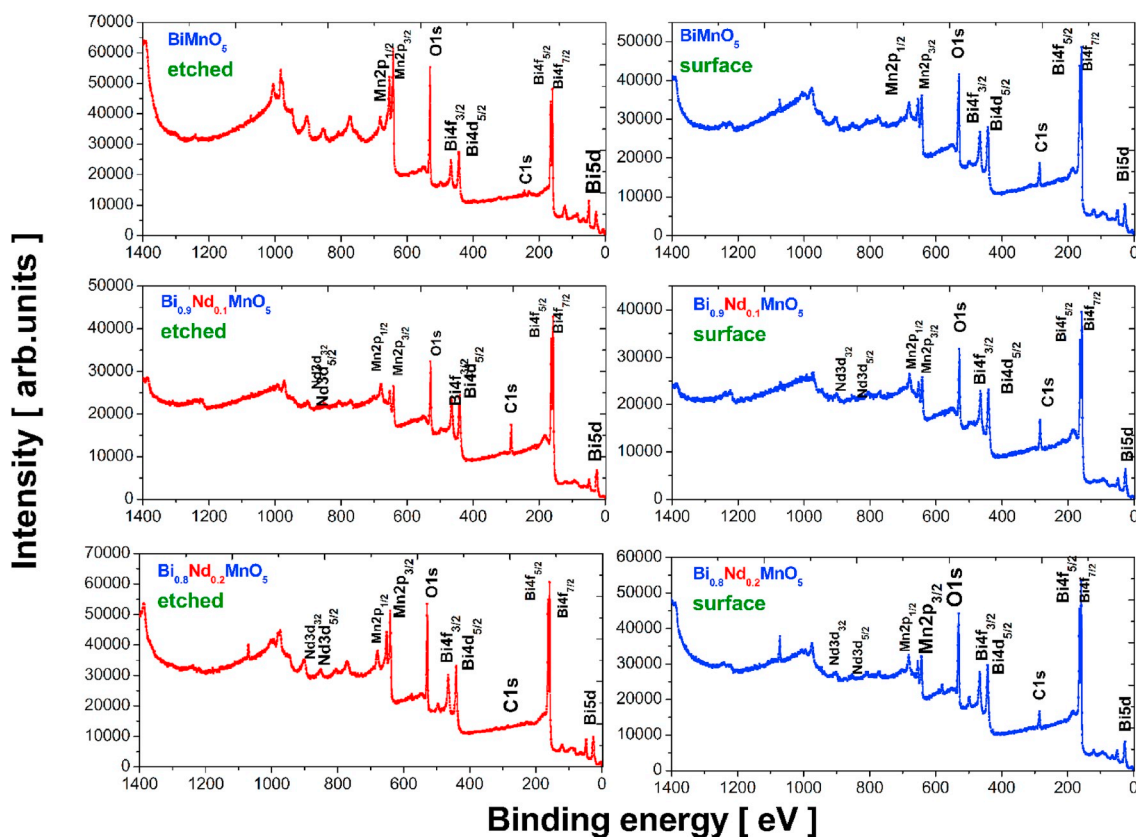**Fig. 5.** The IR spectra at room temperature for all samples.

Fig. 6. XPS spectra for binding energies of $Bi_{1-x}Nd_xMn_2O_5$ (x = 0 m 0.1 and 0.2 0:2) before and after etched for 30 min.
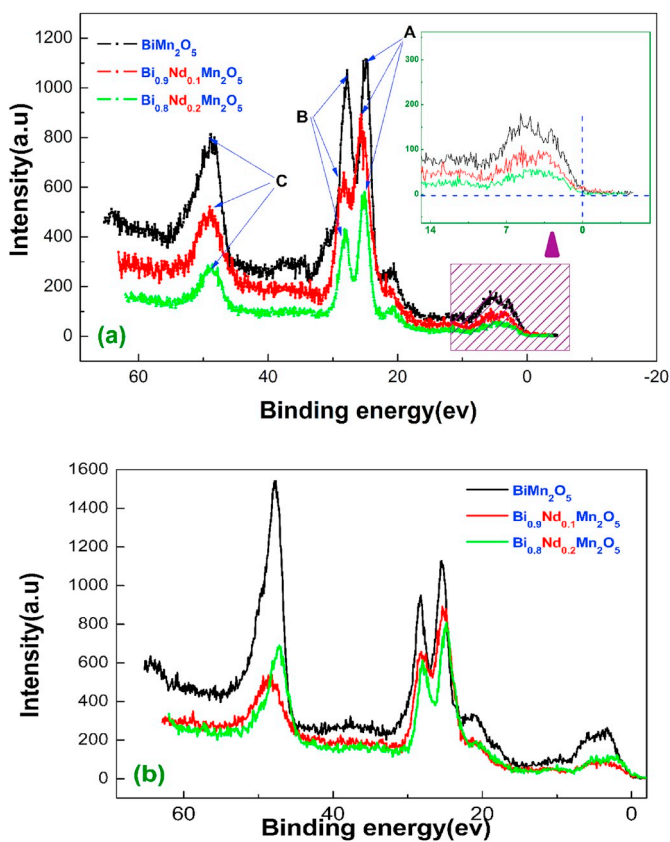

Fig. 7. XPS of the valence band of all samples (a) before etching and (b) after etching.

It consists of two main peaks (A and B) which represent Bi 5d states (A - $Bi5d_{5/2}$ and B - $Bi5d_{3/2}$) with the spin – orbit splitting of about $\Delta E \approx 2.9$ eV and partly overlapped with O 2s states visible above 20 eV as small shoulder of A peak. The line (C) represents the contribution from Mn3p states. The shapes of the energy positions of the XPS spectrum VB of all the features after etching are in very good agreement with the XPS spectrum VB before etching, Fig. 7. (b). The Fermi level E_F was defined with the accuracy of 0.127, 0.32 and 0.48 eV for $BiMn_2O_5$, $Bi_{0.9}Nd_{0.1}Mn_2O_5$ and $Bi_{0.8}Nd_{0.2}Mn_2O_5$ respectively. The inset of Fig. 7(a) shows the near E_F region of VB.

The high-resolution spectra of the Bi4f, Mn2p and Nd3d regions were recorded by XPS and fitted using mixed Gauss – Lorentz functions and with the use of Shirley background. Fig. 8 shows the XPS core level spectra for the binding energy of Bi in $Bi_{1-x}Nd_xMn_2O_5$(x = 0, 0.1 and 0.2) before and after etching. The chemical shifts are well visible. It is observed, that Bi 4f lines are usually composed of four peaks typical for pure Bi as well as Bi_2O_3 states. One may noting that the energy positions for Bi 4f spectra is rather stable before and after cleaning procedure. For the $Bi_{1-x}Nd_xMn_2O_5$ (x = 0 and 0.1) samples each line Bi4f line can be fitted with two components (Bi^{3+} and Bi_2O_3). We assert that in the case of x = 0.1 sample the second component at slightly lower binding energy is also Bi^{3+} in a different chemical environment [31,32]. On the other hand, for $Bi_{0.8}Nd_{0.2}Mn_2O_5$ is modeled by one component (Bi_2O_3), but after cleaning the surface for 30 min with the use of Ar^+ beam the pure Bi states are well visible.

Fig. 9 shows the XPS spectra for the binding energy of Mn2p states in $BiMn_2O_5$, $Bi_{0.9}Nd_{0.1}Mn_2O_5$ and $Bi_{0.8}Nd_{0.2}Mn_2O_5$. The Mn2p was split by the spin–orbit interactions into the Mn $2p_{3/2}$ and Mn $2p_{1/2}$ peaks. The Mn $2p_{3/2}$ peak is deconvoluted into corresponding of Mn^{3+} and Mn^{4+} peaks with the binding energy of 640 eV and 642 eV, respectively [33,34]. Our broad Mn $2p_{3/2}$ line obviously shows an overlapping of Mn^{3+} $2p_{3/2}$ and Mn^{4+} $2p_{3/2}$ lines, which indicative of the coexistence of Mn^{3+} and Mn^{4+} ions. Comparing the area under each curve, it can
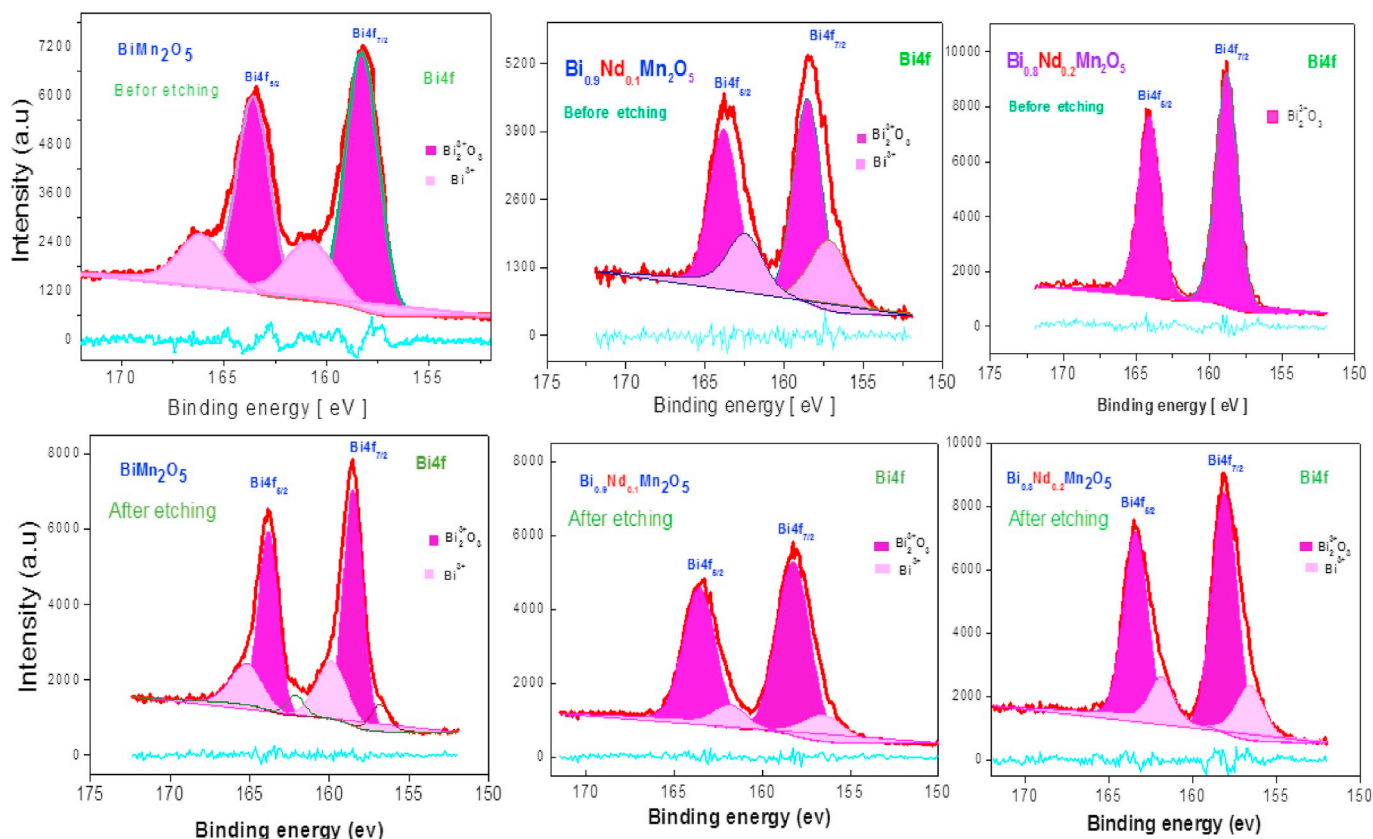
Fig. 8. XPS spectra for [Bi $4f_{5/2}$, Bi $4f_{7/2}$] of Bi^{3+} and Bi_2O_3 for all samples before and after etched for 30 min.
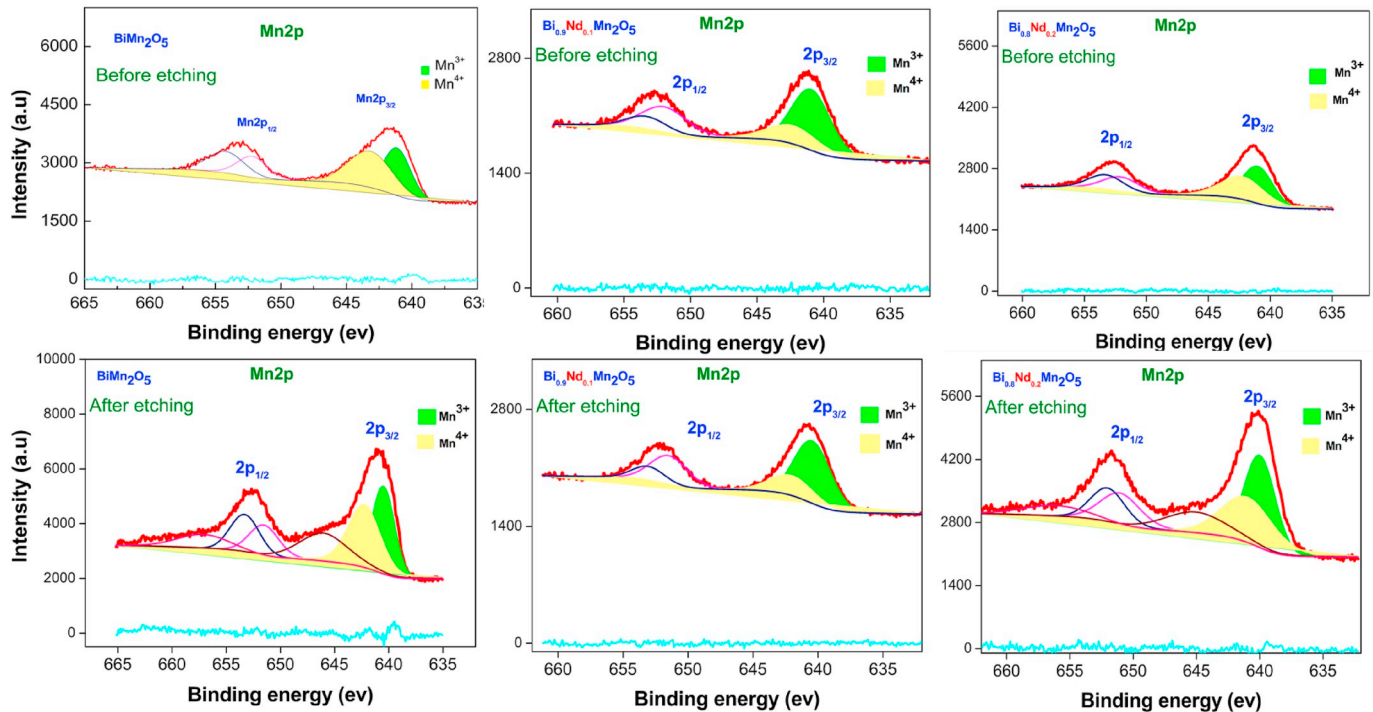

Fig. 9. XPS spectra for [Mn $2p_{1/2}$, Mn $2p_{3/2}$] of Mn^{3+} and Mn^{4+} for all samples before and after etched for 30 min.
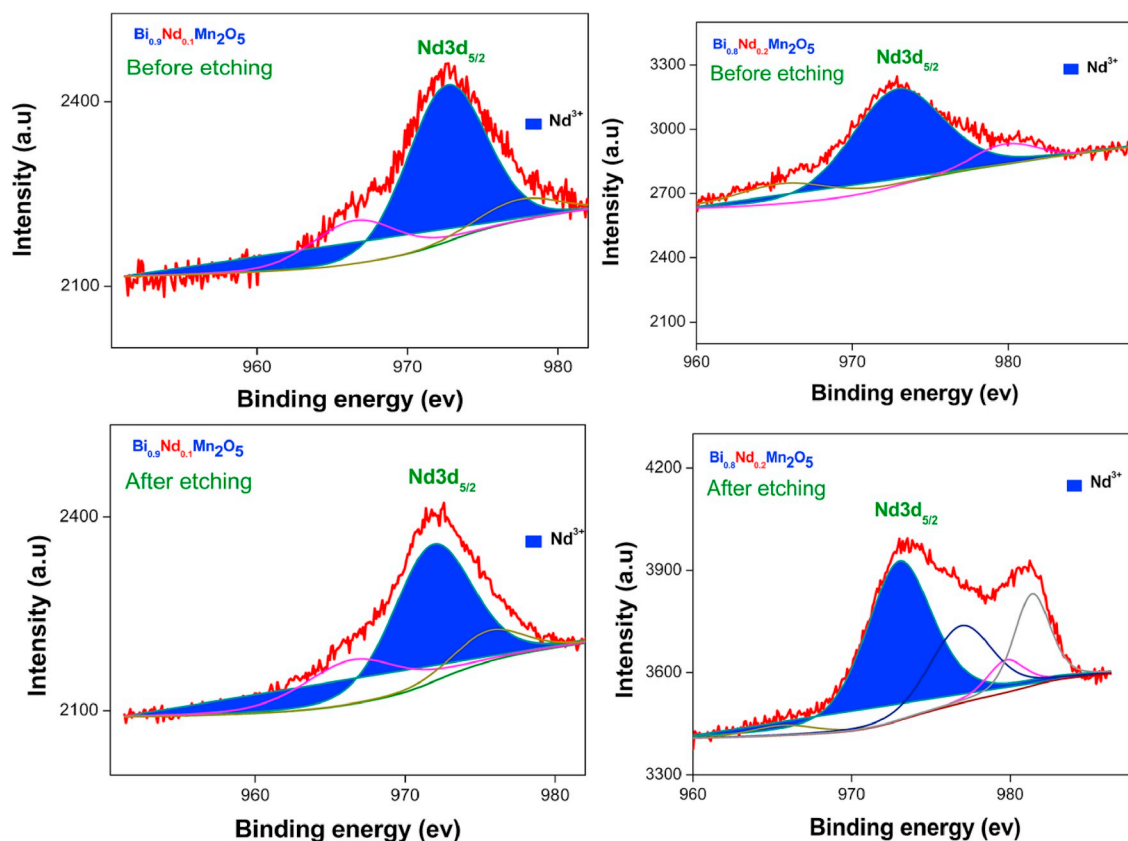
Fig. 10. XPS spectra for [Nd3d $_{5/2}$] of Nd^{3+} for $Bi_{0.9}Nd_{0.1}Mn_2O_5$ and $Bi_{0.8}Nd_{0.2}Mn_2O_5$ before and after etched for 30 min.

Table 5
Binding energies of Bi4f and Mn2p for BiMn2O5 sample before and after etching for 30 min.

$BiMn_2O_5$	Bi4f		Mn2p
	Positon	%Gauss	Positon
Before etching	158.26	100	641.14
	160.83	91	643.16
	163.57	100	652.19
	166.14	74	654.21
After etching	156.82	78	641.50
	158.52	98	642.24
	159.87	90	646.05
	162.13	77	651.55
	163.83	100	653.29
	165.18	90	657.10

Table 6
Binding energies of Bi4f, Mn2p and Nd3d$_{5/2}$ for Bi$_{0.9}$Nd$_{0.1}$Mn2O5 sample before and after etching for 30 min.

$Bi_{0.9}Nd_{0.1}Mn_2O_5$	Bi4f		Mn2p	Nd3d$_{5/2}$
	Positon	%Gauss	Positon	Positon
Before etching	157.14	91	640.93	966.50
	158.50	100	642.25	972.58
	162.45	89	651.98	977.40
	163.81	100	653.30	
After etching	156.56	78	640.43	966.50
	158.23	98	642.00	971.79
	161.87	71	651.48	975.58
	163.54	97	653.05	

be concluded that Mn^{3+} state is the highest valence state in these samples. So, the shapes of the energy positions of the Mn2p XPS spectrum of all samples after etching are in accordance with the Mn2p XPS spectrum before etching. As shown by the XPS spectra of Nd in Fig. 10, since only the Nd^{3+} ionic state is formed, Nd exhibits a sharp spectrum before etching for $Bi_{0.9}Nd_{0.1}Mn_2O_5$ and $Bi_{0.8}Nd_{0.2}Mn_2O_5$. The shape of the energy positions of the Nd 3d$_{5/2}$ XPS spectrum of $Bi_{0.9}Nd_{0.1}Mn_2O_5$ sample after etching accords well with the spectrum Nd 3d$_{5/2}$ XPS before etching. However, for the compound $Bi_{0.8}Nd_{0.2}Mn_2O_5$ after etching the surface at 30 min with the use of Ar^+ beam, it is observed that the content of the functional group in the Nd 3d$_{5/2}$ increases. The resulting peak positions under the peaks determined from this fitting for each spectra are given in Tables 5–7.

3.5. Magnetic measurements

As shown in Fig. 11, the dc magnetic magnetization of $BiMn_2O_5$ and $Bi_{0.8}Nd_{0.2}Mn_2O_5$ as a function of temperature in three different measurement protocols viz: zero-field cooled (ZFC), field-cooled cooling (FCC) and field cooled warming (FCW) conditions measured under an applied magnetic field of 0.5 kOe. T_N = (31 K and 61 K), showing AFM coupling between Mn-spins corresponding to the temperature of divide between ZFC and FCC measurements. The curves of inverse magnetic susceptibility for both samples at the paramagnetic state are shown in Fig. 11. The analysis of $1/\chi$ vs T by linear regression in the range [100–300 K] allows finding the paramagnetic Curie temperature θ_p and the constant of Curie C for both samples, with the values of $\theta p = (-241.59, -212K)$ and C = (4.86854 , 5.151983Oe. K. mol. emu^{-1}) for $BiMn_2O_5$ and $Bi_{0.8}Nd_{0.2}Mn_2O_5$, respectively.

Table 7

Binding energies of Bi4f, Mn2p and Nd3d$_{5/2}$ for Bi$_{0.9}$Nd$_{0.1}$Mn2O5 sample before and after etching for 30 min.

Bi$_{0.8}$Nd$_{0.2}$Mn$_2$O$_5$	Bi4f		Mn2p	Nd3d$_{5/2}$
	Positon	%Gauss	Positon	Positon
Before etching	158.80	85	641.01	965.60
	164.11	83	642.19	972.81
			652.06	979.78
			653.24	
After etching	156.56	70	640.00	965.67
	158.09	100	640.96	972.99
	161.87	70	645.05	976.89
	163.40	99	651.05	979.72
			652.01	981.37
			656.10	1002.32

The temperature-dependent magnetic magnetization as a function of temperature in three different measurement protocols viz: zero-field cooled (ZFC), field-cooled cooling (FCC) and field-cooled warming (FCW) conditions and inverse susceptibility for $Bi_{0.9}Nd_{0.1}Mn_2O_5$ is presented in Fig. 12. At low temperatures, the magnetization increases and exhibits an outspread maximum with two characteristic temperatures T = 32 K and T = 40 K, which would suggest the appearance of an AFM order with T$_N$ = 40 K. The existence of two transition temperatures

could indicate a small delay in the ordering of the magnetic moments associated with one of the manganese sites with respect to the second one. The evolution of the ZFC and the FC curves is very similar [35], which seems to exclude the presence of weak ferromagnetism effects [35]. According to the Curie-Weiss (CW) $\chi = \frac{C}{T - \theta_p}$ fitting, we can obtain C = (5.0602165 Oe.K.mol.uem^{-1}) and $\theta p = -236.14K$. We observed that the Curie constants increase with the increase in Nd^{3+} content. The negative values for the paramagnetic curie temperatures indicate that the magnetic interaction is predominately-antiferromagnetic [36].

From the fitted value of the Curie constant C, effective paramagnetic moment value of $\mu = 6.2408$, $6.36525 and$ 6.4199 μ_B were derived for $Bi_{1-x}Nd_xMn_2O_5$ with (x = 0, 0.1 and 0.2) respectively. According to the general understanding supported by our XPS results reported above, the ionic structure of the orthorhombic manganite is $Bi_{1-x}^{3+}Nd_x^{3+}Mn^{3+}Mn^{4+}O_5$. In a paramagnetic state, the magnetic moment per structural unit can be expressed with the magnetic moments of individual ions [37–39]:

$$\mu(Bi_{1-x}Nd_xMn_2O_5) = [x\mu(Nd^{3+})^2 + (1-x)\mu(Mn^{3+})^2 + (1+x)\mu(Mn^{4+})^2]^{1/2}$$

(7)

where Bi^{3+} ions have no magnetic moment since they do not have unpaired d- or f-electrons, therefore, the magnetic state in those compounds is determined uniquely by the Mn^{4+}, Mn^{3+} and Nd^{3+} ions subsystems. The theoretical paramagnetic moment is given by:
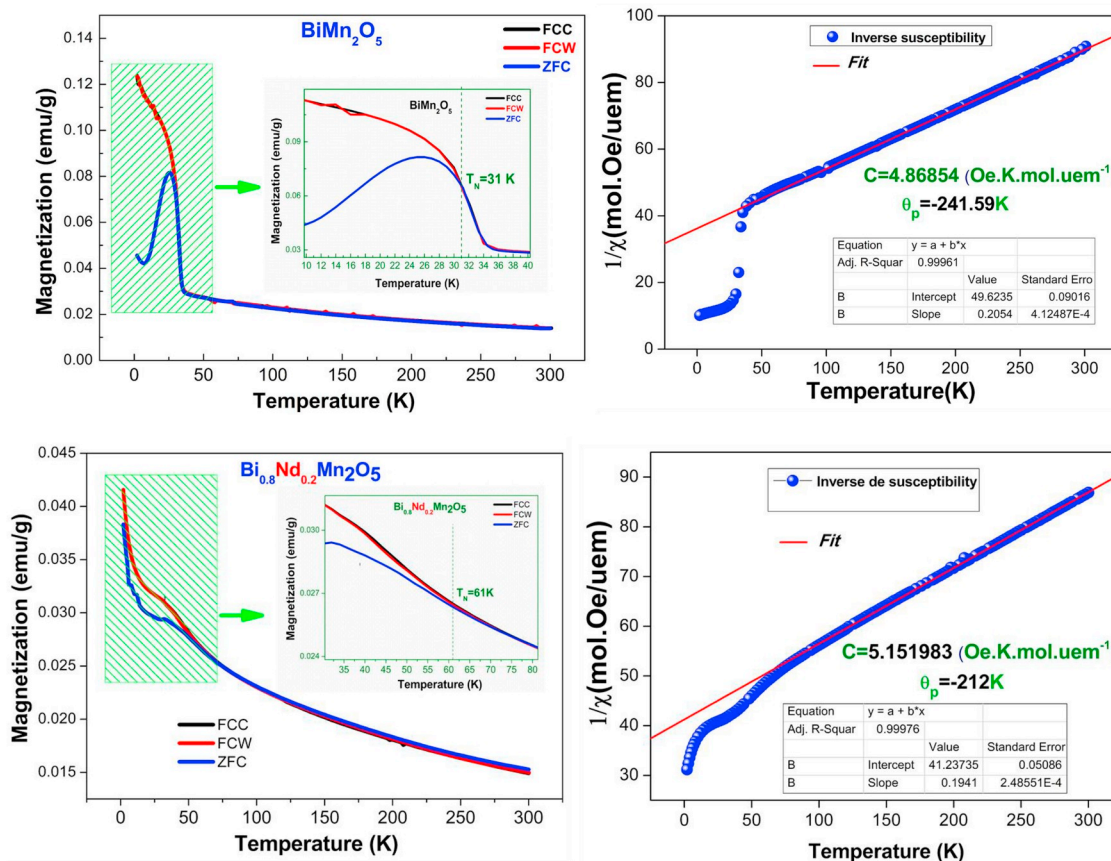

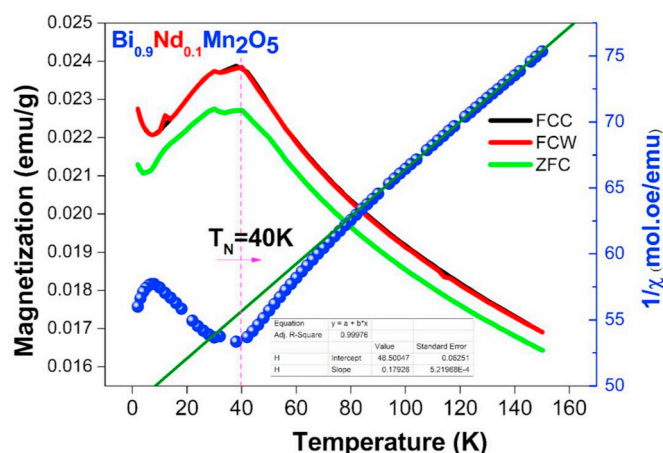**Fig. 11.** FCC, FCW and ZFC curves and the inverse susceptibility for (a) BiMn2O5 and (b) Bi0.8Nd0.2Mn2O5.

Fig. 12. FCC, FCW and ZFC curves for Bi0.9Nd0.1Mn2O5. Also shown is the inverse susceptibility of the FC curve.

$$\mu = g_J([J(J+1)])^{1/2} \tag{8}$$

where J is ion's total moment and g is a Lande g-factor determined as:

$$g = 1 + \frac{J(J+1) + S(S+1) - L(L+1)}{2J(J+1)} \tag{9}$$

with S and L being ion's spin and orbital moments. The magnetic moments of the manganese neodyme ions calculated with (8) in this approximation are $\mu(Mn^{3+}) = 4.90\,\mu_B$, $\mu(Mn^{4+}) = 3.87\mu_B$ and $\mu(Nd^{3+}) = 3.62\,\mu_B$. The effective magnetic moment is in good agreement with the theoretical values, of 6.24, 6.27 and 6.30 for $Bi_{1-x}Nd_xMn_2O_5$ with (x = 0, 0.1 and 0.2), respectively. Our experimental μ_{eff} value shows the coexistence of Mn^{3+} and Mn^{4+} in $Bi_{1-x}Nd_xMn_2O_5$. Therefore, XPS and the magnetic moment both indicate the coexistence of mixed Mn^{3+} and Mn^{4+} valences [39] At low temperatures, a weak ferromagnetic state caused by Mn arrays is observed [35].

The isothermal magnetization curves of all samples displayed in Fig. 13(a), (b) and (c) show a negligible magnetization at low temperatures, discarding the presence of a weak ferromagnetism effect. The hysteresis loops observed at different temperatures are found in the inset of these figures. For 5 K, the coercive field for $BiMn_2O_5$, $Bi_{0.9}Nd_{0.1}Mn_2O_5$ and $Bi_{0.8}Nd_{0.2}Mn_2O_5$ are 676, 128 and 106 Oe, respectively, is observed due to a weak ferromagnetic state caused by Mn gratings. The replacement of Bi^{3+} by Nd^{3+} favored a decrease in the coercive field and an increase in the T_N, suggesting weak ferromagnetic property, which is canted-antiferromagnetic coupling.

4. Conclusion

We have synthesized multiferroic samples with (x = 0, 0.1 and 0.2) by sol gel method. The XRD pattern resulted in crystallizing in a mullite-type orthorhombic perovskite structure, space group *Pbam* (Z = 4). Scanning electron microscopy (SEM) has revealed that the grains are irregularly spherical-like shaped confirming the formation of single-phase materials with excellent mapping distribution, with mean sizes of 107, 103 and 92 for (x = 0, 0.1 and 0.2), respectively. The replacement of Bi^{3+} by Nd^{3+} favored not only a decrease in the average crystallite size calculated using the Scherer formula, but also in the grain size estimated by SEM. XPS and the magnetic moment both indicate the coexistence of mixed Mn3+ and Mn4+ valences.
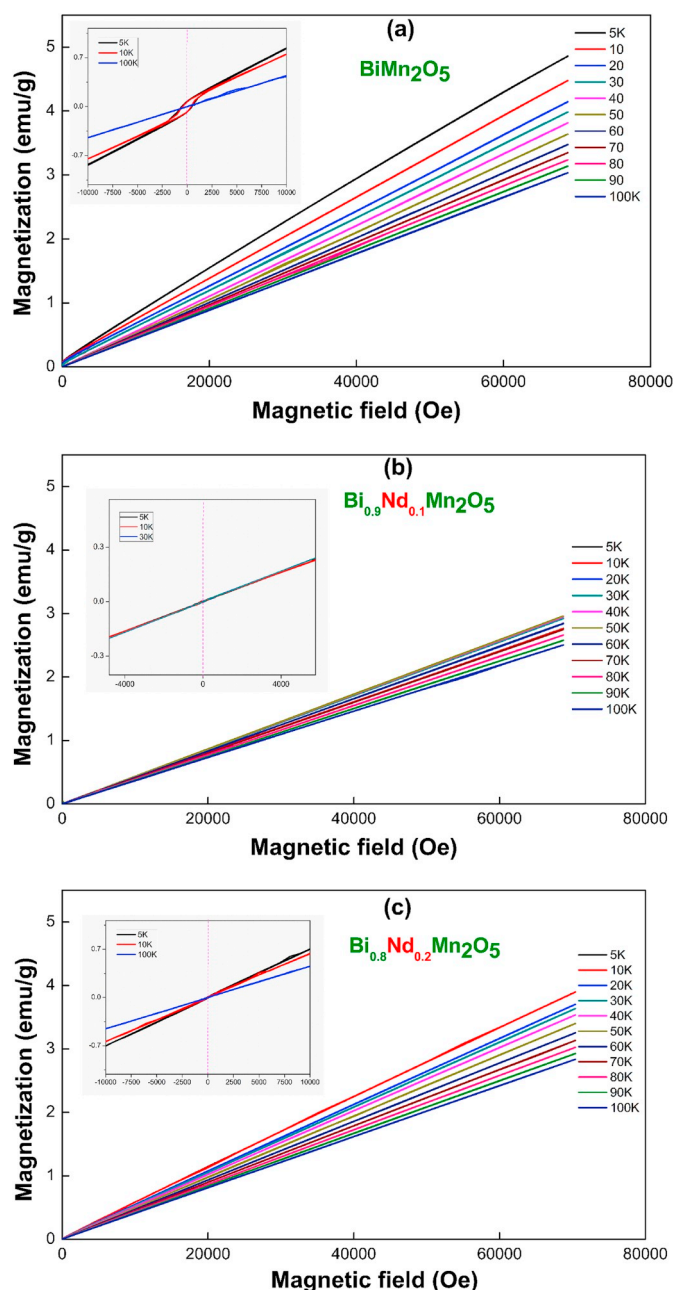

Fig. 13. Field-dependent magnetization measured at different temperatures. The inset are magnetic hysteresis of all samples.

Prime novelty statement

In the present study a novel series of multiferroic materials $BiMn_2O_5$ doped by Neodyme has been prepared by a sol-gel method at low temperature. Rietveld refinement of the room temperature X-ray diffraction data indicates that this system is characterized by a single phase and crystallizes in the orthorhombic structure with space group *Pbam*. Scanning electron microscopy (SEM) revealed that the grains are irregularly spherical-like shaped confirmed the formation of single-phase materials with excellent mapping distribution, with mean sizes of

107, 103 and 92 for (x = 0, 0.1 and 0.2) respectively. The replacement of Bi^{3+} by Nd^{3+} favored a decrease in the average crystallite size was calculated using the Scherer formula as well, a decrease in grain size estimated by SEM. XPS and the magnetic moment both indicate the coexistence of mixed Mn^{3+} and Mn^{4+} valences.

Acknowledgements

Appendix A. Supplementary data

Supplementary data to this article can be found online at https://doi.org/10.1016/j.pnsc.2019.04.001.

References

[1] Y. Tokura, S. Seki, J. Adv. Mater. 22 (2010) 1554.
[2] R.M. Kenzelmann, A.B. Harris, S. Jonas, C. Broholm, J. Schefer, S.B. Kim, C.L. Zhang, S.-W. Cheong, O.P. Vajk, J.W. Lynn, J. Phys. Rev. Lett. 95 (2005) 087206.
[3] N. Ikeda, H. Ohsumi, K. Ohwada, K. Ishii, T. Inami, K. Kakurai, Y. Murakami, K. Yoshii, S. Mori, Y. Horibe, H. Kitô, Nature 436 (2005) 1136.
[4] N. Hur, S. Park, P.A. Sharma, J. Ahn, S. Guha, S.-W. Cheong, Nature 429 (2004) 392.
[5] Rafael A. Ferreira, Maria Elenice dos Santos, Cássio Morilla-Santos, Ronan Lebullenger, Octavio Peña, Paulo Noronha Lisboa-Filho, J. Ceram. Int. 40 (2014) 13643.
[6] T. Doi, K. Kohn, Phase Transitions 38 (1992) 273.
[7] H. Tsujino, K. Kohn, J. Solid State Commun. 83 (1992) 639.
[8] Y. Tanaka, K. Saito, H. Tsujino, K. Kohn, J. Ferroelectr. 161 (1994) 125.
[9] K. Saito, K. Kohn, J. Phys. Condens. Matter 7 (1995) 2855.
[10] K.S. Kumar, C. Venkateswaran, J. Phys. D 44 (2011) 325001.
[11] A. Muñoz, J.A. Alonso, M.T. Casais, M.J. MartínezLopez, J.L. Martínez, M.T. Fernadez-Díaz, J. Phys. Rev. B 65 (2002) 1444423.
[12] Weiwei Mao, Wei Chen, Xingfu Wang, Yiyi Zhu, Yuhui Ma, Hongtao Xue, Liang Chu, Jianping Yang, Xing'ao Li, Wei Huang, J. Ceram. Int 42 (2016) 12838.
[13] T. Wang, S. Song, M. Wang, J. Li, M. Ravi, J. Ceram. Int. 42 (2016) 7328–7335.
[14] H. Felhi, R. Lahouli, M. Smari, H. Rahmouni, K. Khirouni, E. Dhahri, J. Mol. Struct. 1179 (2019) 1.
[15] Rodriguez-Carvajal, J. Phys. B 192 (1993) 55.
[16] H.M. Rietveld, J. Appl. Crystallogr. 2 (1969) 65.
[17] A. Muñoz, J.A. Alonso, M.J. Martínez-Lopez, J.L. Martínez, J. Phys. Rev. B 72 (2005) 184402.
[18] A. Muñoz, J.A. Alonso, M.T. Casais, M.J. Martínez Lopez, J.L. Martínez, M.T. Fernadez-Díaz, Eur. J. Inorg. Chem. 4 (2005) 685.
[19] J.A. Alonso, M.T. Casais, M.J. Martínez-Lopes, J.L. Martínez, M.T. Fernández-Díaz, J. Phys. Condens. Matter 9 (1997) 8515.
[20] Lija K. Joy, M.R. Senoy Thomas, J. Anantharaman, Magn. Magn. Mater. 09 (2015) 020.
[21] S.R. Mohapatra, A. Swain, C.S. Yadav, S.D. Kaushik, A.K. Singh, J. RSC Adv. 6 (2016) 112282.
[22] A.J.C. Wilson, J. Acta Cryst. 14 (1961) 696.
[23] S.V. Trukhanov, A.V. Trukhanov, S.G. Stepin, H. Szymczak, C.E. Botez, J. Phys. Solid State 50 (2008) 886.
[24] Azhar Mahmood, Muhammad Farooq Warsi, Muhammad NaeemAshiq, Muhammad Ishaq, J. Magn. Magn. Mater. 372 (2010) 64.
[25] Vaishali V. Soman, V.M. Nanoti, D.K. Kulkarni, Vijay V. Soman, J. Phys. Proc. 54 (2014) 30.
[26] S.M. Borchani, W.C-R. Koubaa, M. Megdiche, R. Soc. Open Sci. 4 (11) (2017) 170920.
[27] D.L. Rousseau, R.P. Bauman, S.P.S. Porto, J. Raman Spectrosc. 10 (1981) 253.
[28] D.K. Shukla, Ravi Kumar, S. Mollah, R.J. Choudhary, P. Thakur, S.K. Sharma, N.B. Brookes, M. Knobel, J. Phys. Rev B. 82 (2010) 174432.
[29] S. Chauhan, M. Kumar, S. Chhoker, S.C. Katyal, M. Singh, J. RSC Adv. 6 (2016) 43080.
[30] A.F. García-Flores, E. Granado, H. Martinho, R.R. Urbano, C. Rettori, E.I. Golovenchits, V.A. Sanina, S.B. Oseroff, S. Park, S.-W. Cheong, J. Phys. Rev. B 73 (2006) 104411.
[31] Paul F. Newhouse, Sebastian E. Reyes-Lillo, Guo Li, Lan Zhou, Aniketa Shinde, Dan Guevarra, Santosh K. Suram, Edwin Soedarmadji, Matthias H. Richter, Xiaohui Qu, Kristin Persson, Jeffrey B. Neaton, John M. Gregoire, J. Chem. Mater. 29 (2017) 10027.
[32] T. Ogawa, H. Shindo, H. Takeuchi, Y. Koizumi, Jpn. J. Appl. Phys. 45 (2006) 8666.
[33] J. Wei, D. Xue, C. Wu, Z. Li, J. Alloy. Compd. 453 (2008) 20.
[34] C.F. Chung, J.P. Lin, J.M. Wu, Appl. Phys. Lett. 88 (2006) 242909.
[35] J.A. Alonso, M.T. Casais, M.J. Martı´nez-Lope, J.L. Martı´nez, J. Phys. Rev. B 65 (2002) 144423.
[36] Z.H. Sun, B.L. Cheng, S. Dai, K.J. Jin, Y.L. Zhou, H.B. Lu, Z.H. Chen, G.Z. Yang, J. Appl. Phys. 99 (2006) 084105.
[37] I.E. Chupis, Fiz. Nizk. Temp. 36 (2010) 597.
[38] P.W. Selwood, Magnetochemistry, Interscience Publisher, New York/London, 1958.
[39] R.L. Karlin, Magnetochemistry, Nauka, Moscow, 1989.